

Gold, Platinum, and Aluminum Nanodisk Plasmons: Material Independence, Subradiance, and Damping Mechanisms

Igor Zorić, Michael Zäch, Bengt Kasemo, and Christoph Langhammer*

Department of Applied Physics, Division for Chemical Physics, Chalmers University of Technology, 412 96 Göteborg, Sweden

Localized surface plasmon resonances (LSPR) are collective electronic oscillations in metallic nanoparticles and can be resonantly excited by external electric fields.^{1,2} They have been explored extensively in terms of their fundamental properties as well as for a plethora of possible applications in, just to name a few, optoelectronic devices,³ optical metamaterials,^{4,5} sensors,^{6,7} and solar cells.⁸ During the past decade's concomitant rapid development of "plasmonics" into a vibrant sub-area of nanotechnology, the focus was almost entirely on Au and Ag as (nano)-plasmonic metals. This preference was motivated by the distinct dielectric properties of Au and Ag in the vis–NIR spectral range. In particular, the low intrinsic losses through intraband excitations at energies just below the interband absorption threshold, which are related to the position of the d bands with respect to the Fermi level, make Ag and Au very attractive plasmonic metals. Nevertheless, other metals, which have not yet received comparable attention as nanoplasmonic materials, have recently been shown to provide interesting novel combinations of intrinsic material properties (e.g., catalytic activity, oxide formation, hydride formation, magnetic properties, etc.) with the possibility to excite LSPR and the concomitant possibility to, for example, explore these LSPR excitations as transducers in novel nanoplasmonic sensing schemes.^{7,9–14} Significantly different bulk dielectric properties, compared to Ag and Au, characterize these "novel" plasmonic metals, often deriving from the presence of relatively strong interband activity over a wide frequency range and concomitant damping. It is therefore highly relevant, both fundamentally and in view of applications, to scrutinize how the most important features of the bulk dielectric properties of these novel nanoplasmonic systems are

ABSTRACT Localized surface plasmon resonances (LSPR) are collective electronic excitations in metallic nanoparticles. The LSPR spectral peak position, as a function of nanoparticle size and material, is known to depend primarily on dynamic depolarization and electron structure related effects. The former gives rise to the well-known spectral red shift with increasing nanoparticle size. A corresponding understanding of the LSPR spectral line width for a wide range of nanoparticle sizes and different metals does, however, not exist. In this work, the radiative and nonradiative damping contributions to the LSPR line width over a broad nanoparticle size range (40–500 nm) for a selection of three metals with fundamentally different bulk dielectric properties (Au, Pt, and Al) are explored experimentally and theoretically. Excellent agreement was obtained between the observed experimental trends and the predictions based on electrostatic spheroid theory (MLWA), and the obtained results were successfully related to the specific band structure of the respective metal. Moreover, for the first time, a clear transition from a radiation damping dominated to a quenched radiation damping regime (subradiance) in large nanoparticles was observed and probed by varying the electron density through appropriate material choice. To minimize inhomogeneous broadening (commonly present in ensemble-based spectroscopic measurements), a novel, electron-beam lithography (EBL)-based nanofabrication method was developed. The method generates large-area 2D patterns of randomly distributed nanodisks with well-defined size and shape, narrow size distribution, and tunable (minimum) interparticle distance. In order to minimize particle–particle coupling effects, sparse patterns with a large interparticle distance (center-to-center ≥ 6 particle diameters) were considered.

KEYWORDS: localized surface plasmon resonance · line width · plasmon energy · gold · platinum · aluminum · subradiance · material independence

reflected in their LSPR excitations over a wide nanoparticle size and spectral range.

Generally speaking, the spectral line shape of the LSPR in any metallic nanosystem, as obtained when measuring extinction, absorption, or scattering cross sections as a function of photon energy, can be characterized by the spectral peak position (peak energy) and the resonance line width (full width at half-maximum, fwhm), assuming heterogeneous broadening is small or absent. It is well-established that the LSPR peak position, as a function of nanoparticle size and material (*i.e.*, the dielectric response function), primarily depends

* Address correspondence to clangham@chalmers.se.

Received for review August 26, 2010 and accepted March 25, 2011.

Published online March 25, 2011
10.1021/nn102166t

© 2011 American Chemical Society

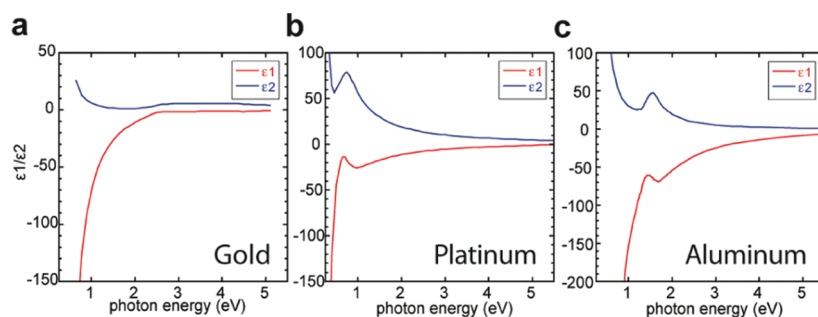


Figure 1. Dielectric functions of bulk (a) gold,³³ (b) platinum,³⁴ and (c) aluminum.³⁵

on the bulk plasmon energy, ω_p (i.e., electron density), and dynamic depolarization effects.^{15,16} The depolarization gives rise to the well-known spectral red shift of the LSPR peak position with increasing nanoparticle diameter for nanoparticles with identical geometry.

A corresponding understanding of the LSPR line width over a wide spectral range (UV–vis–NIR) is, however, not available for a wide range of nanoparticle sizes and different metals. The latter is yet essential since damping processes, which limit the coherent lifetime and thus the “quality factor” and local field enhancement of the plasmonic oscillations, play an important role in numerous applications like enhanced spectroscopy,¹⁷ sensing,^{6,7} photovoltaics,⁸ photocatalysis, and plasmonic heating¹⁸ (a more detailed discussion of such aspects is given in the Perspective section below). In this study, we present general qualitative arguments (supported and quantified by detailed experimental and theoretical analysis of the three particular systems Au, Pt, and Al) which can be used in a very general way to understand and predict the nanoplasmonic properties in terms of plasmon energy and damping mechanisms for basically any (potentially technologically important) metallic nanosystem with known bulk dielectric properties.

BACKGROUND

In principle, both radiative and nonradiative damping processes are present in nanoparticles larger than 20–30 nm, and the LSPR line width is affected by both decay channels. Their absolute and relative contributions are both particle size and material dependent. The radiative damping is related to the energy losses caused by photon emission and has been shown to increase with nanoparticle size.¹⁹ The nonradiative damping involves intraband excitations (electron scattering processes within the nanoparticle) and interband excitations leading, at first, to the formation of one excited electron–hole pair. The latter generates, *via* a cascade process, a multitude of e–h pairs eventually having energies approaching the phonon “bath” and thus eventually leading to the generation of heat.²⁰ Nonradiative damping is primarily determined by the electronic structure of the metal *via* its dielectric function, which contains contributions from both intraband and

interband excitations. In the context of applications, especially for photon harvesting, it is worth noting that damping *via* the e–h pair cascade in the plasmonic particle leads to an irreversible loss of the photon, while radiation can lead to a new excitation in another plasmonic particle or an adjacent semiconductor.

To address the issues introduced above, several different experimental attempts have been made using various approaches to scrutinize the LSPR line width as a function of nanoparticle size. A commonly used approach involves studies of electron-beam lithography (EBL) fabricated, ordered arrays of particles with narrow size distribution to minimize the inhomogeneous broadening of the LSPR.^{21,22} Measurements on such structures in the frequency domain thus reveal the line width's size dependence reasonably well. Earlier studies were, however, often carried out for narrow particle size ranges only and restricted to Au and Ag for various reasons.

Hole-mask colloidal lithography²³ is an alternative and fast nanofabrication method, which has been successfully used to prepare random nanoparticle arrangements of different metals covering a wide size range from 35 to 500 nm and to study their plasmonic properties in detail.^{11,24,25} However, measurements of LSPR line widths suffered from quite severe inhomogeneous broadening effects related to the broad particle size distribution characteristic of this preparation method, in particular for small particle sizes.

In contrast to the ensemble-based approaches mentioned above, single particle studies relying on dark-field scattering spectroscopy of colloidal particles and EBL fabricated structures efficiently avoid ensemble averaging. Using such an approach, interesting effects like the drastic reduction of the plasmon dephasing rate in nanorods as compared to small nanospheres due to the suppression of interband damping have been observed for a limited size range of Au nanoparticles.²⁶ In another work, Hu *et al.* used dark-field scattering spectroscopy on Au nanorods, Au–Ag nanoboxes, and Au–Ag nanocages to study electron–surface scattering and radiation damping for particles in the few tens of nanometer size range.²⁷

However, the available spectral range typically limits such studies, and the method is very inefficient for

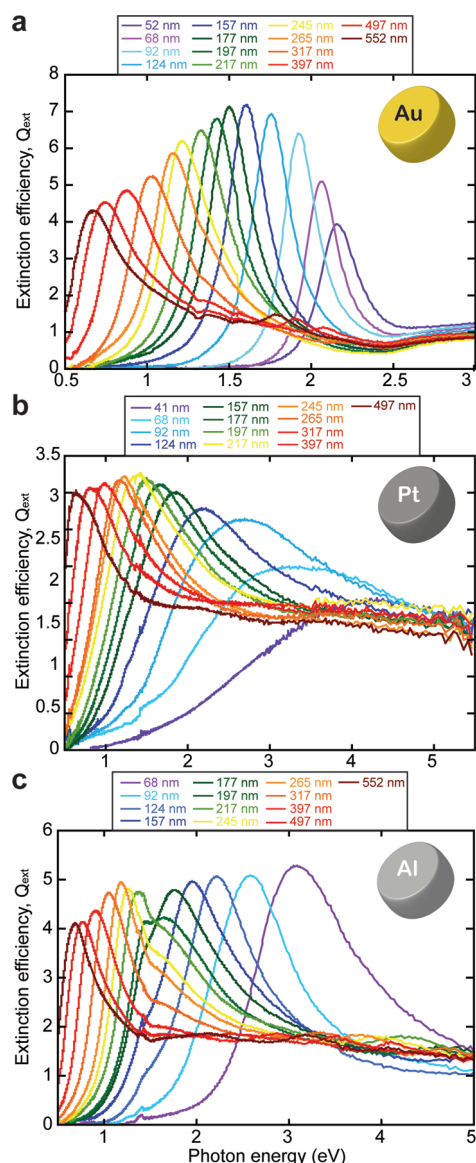


Figure 2. Experimentally measured extinction efficiency spectra for random arrays of Au (a), Pt (b), and Al (c) nanodisks fabricated by our novel EBL-based approach. The smallest allowed particle–particle (center to center) distance in the arrays was 6 nanodisk diameters.

materials in which LSPR predominantly decays through nonradiative channels. Using scanning near-field optical microscopy (SNOM), spectral hole burning, and pulse-probe techniques (in the time domain), measurements of the line width of single nanoparticles have also been achieved for a limited particle size range.^{28–30} The specific role of interband excitations in LSPR damping has so far, to the best of our knowledge, only been addressed experimentally by looking at LSPR line widths in nanoshells made from coinage metals.³¹

The main purpose of the present work is therefore to explore experimentally the radiative and nonradiative contributions to the LSPR line width over a broad particle size range (diameter $D = 40\text{--}500\text{ nm}$ at constant height $h = 20\text{ nm}$) for the three plasmonic metals

Au, Pt, and Al with quite different bulk electronic properties. Additionally, the size and material dependence of the LSPR energy will be addressed. To minimize heterogeneous broadening and grating effects, we used a newly developed and EBL-based preparation method allowing patterning of large areas (mm^2) with randomly distributed metal nanodisks with very narrow size distribution on a surface, suitable for extinction spectroscopy in a spectrophotometer with a wide spectral range. Furthermore, the random arrangement together with a large interparticle distance (center-to-center distance ≥ 6 particle diameters) minimizes particle–particle coupling effects and thus make it possible to obtain quasi-single particle information with extinction spectroscopy on EBL fabricated *ensembles* of sparse metallic nanodisks on a surface. The experimental effort is complemented with a theoretical analysis based on the electrostatic spheroid theory in the modified long wavelength approximation (MLWA).^{25,32}

In this context, we note that EBL traditionally has been limited to covering comparably small areas (typically on the order of a few $10\text{ to }100\text{ }\mu\text{m}^2$) with ordered features (e.g., placed on an orthogonal lattice) of interest for nanoplasmonics and that we have circumvented both of these limitations here. Considering that several millions of features have to be exposed when patterning such large areas (i.e., several square millimeters; see the Methods section for details), judicious design of the shot pattern was required in order to limit the writing time to acceptable values. The small but finite beam settling time, which for “traditional” EBL patterns does not contribute significantly to the exposure time, would otherwise have resulted in impractically long writing times. Since the position, size, and shape of a huge number of features have to be generated and stored individually, memory limitations of our EBL system have constituted an additional challenge, which is normally not present if small areas are to be patterned with features on an ordered lattice. This issue was solved by programmatically generating random feature positions within a simulation cell of carefully chosen size and implementing periodic boundary conditions. The size of the simulation cell was chosen such that truly random patterns could be fabricated in a step-and-repeat fashion, while keeping the number of features inside the simulation cell to a minimum.

The three chosen metals, Au, Pt, and Al, constitute an excellent model system, where the interband activity varies greatly and shows the following characteristic features (Figure 1): (a) for Au, a threshold for interband excitation exists at 2.3 eV ; (b) in Pt, interband transitions are an active channel for LSPR decay at all energies (with the top of the occupied $4d$ band at the Fermi energy); and (c) in Al, interband excitations are present only within a narrow energy range (around 1.5 eV due to a pair of parallel bands around the Σ axis on the $\Gamma\text{--K--W--X}$ plane of the Brillouin zone). Furthermore, as another

important difference, we note that the conduction band electron density of Al is 3 times larger than in Au.

RESULTS

In Figure 2, experimentally measured extinction efficiency spectra (*i.e.*, extinction normalized with the projected particle area) for random arrays of Au (a), Pt (b), and Al (c) nanodisks fabricated by our novel EBL-based approach are shown. They reveal significant differences in the overall appearance of the spectra for the different metals, which shall be quantified below.

The experimental data for LSPR peak position (red diamonds) as a function of nanodisk diameter for Au (a), Pt (b), and Al (c) are shown in Figure 3, together with model predictions (blue dots). We find an excellent agreement between the experimental data and the spheroid model calculations over the entire nanodisk size range for all three metals. This observation confirms the anticipated possibility to experimentally obtain quasi-single particle information by extinction spectroscopy on EBL fabricated random arrangements of sparse metallic nanodisks (and strengthens our case when we proceed with the model to interpret the size and material dependence of LSPR damping below). This approach offers the valuable advantage (compared to single particle dark-field scattering experiments) of measurements covering the entire UV–vis–NIR spectral range (and thus large particle size). Additional advantages include the high reproducibility and the possibility to cover comparably large areas with identical nanodisks, which is an essential feature for systematic studies which require a large number of particles in order to provide a measurable response (*e.g.*, reaction products in studies of plasmon-enhanced photocatalysis or photon harvesting in photovoltaics).

Both experimental and theoretical data show a pronounced material dependence of the LSPR energies in the small diameter (D) limit, as shown in Figures 2 and 3. In contrast, in the large D limit, the LSPR energy is essentially material independent and depends only on particle size. The material-specific behavior in the small particle limit is related to the strong dependence of the LSPR energy on electron density (*via* the bulk plasmon energy) and to a smaller extent on differences in the real parts of the dielectric response function for the different metals.

In Figure 4, we show the scaling of experimental and calculated data (using experimental dielectric functions for the respective metals) for the LSPR energy *versus* $1/D$ for the three studied metals. For $D \geq 250$ nm, all of the curves fall on a basically common straight line with a slope of 325 eV nm (Au), 308 eV nm (Pt), and 345 eV nm (Al), if extrapolated through origo.

This material independence of the LSPR energy observed in the large D limit has its origin in the important role of dynamic depolarization. As the

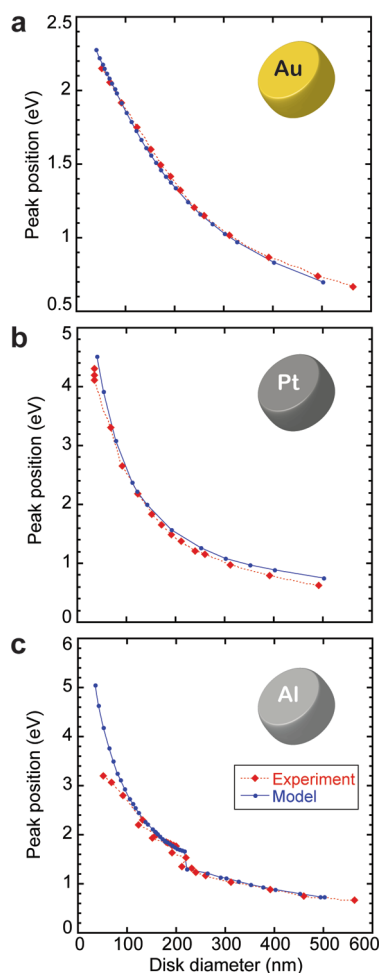


Figure 3. Size dependence of the LSPR peak energy for Au (a), Pt (b), and Al (c) nanodisks with constant height $h = 20$ nm as obtained from extinction measurements. Experimental data (red diamonds) are compared to theoretical values (blue dots), which were obtained using electrostatic spheroid theory (MLWA) as described in the Methods section. The solid/dashed lines are a guide to the eye.

nanodisk diameter increases, the LSPR energy shifts into the red and eventually the period of the collective electron oscillations becomes of the order of the retardation time, $\tau = D/c$, needed to polarize the system (D = nanodisk diameter and c = speed of light). By relying simply on the Heisenberg energy–time uncertainty relation, one can see that the LSPR energy becomes equal (within a factor of n = refractive index of the surrounding medium) to $h/\tau = hc/D$. Thus, with this simple argument, we predict a $1/D$ dependence for the LSPR energy with a slope of $hc = 1239$ eV nm in vacuum or $(1239 \text{ eV nm})/n$ in a medium. We note that this is only an order of magnitude estimate since we do not in any way take into account the nanoparticle geometry. The importance of particle geometry will be highlighted in a more detailed analysis below using the MLWA model where geometry enters both the static and dynamic depolarization prefactors. Nevertheless, the above argument gives a good, simple, and general indication of the origin of the observed

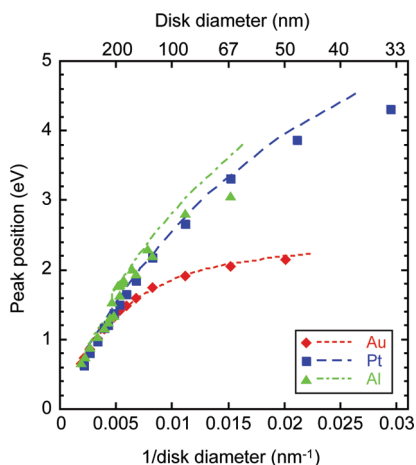


Figure 4. Scaling of the LSPR peak energy with inverse nanodisk diameter. The discrete symbols correspond to experimental data points and the dashed lines to spheroid model calculations. Note the material independent scaling of the peak energy in the limit of large nanodisk diameter (i.e., $D \geq 250$ nm).

material independence and $1/D$ scaling for large nanodisks.

The experimental finding of $1/D$ dependence can be rationalized analytically (in a more system-specific way compared to the very simple derivation above) by relying on the MLWA spheroid model and a Drude description of the metal as follows. The polarizability of an oblate spheroid in the quasistatic limit and in vacuum can be written as¹

$$\alpha(\omega) = \frac{4\pi a^2 b}{3} \frac{\varepsilon(\omega) - 1}{1 + L[\varepsilon(\omega) - 1]} \quad (1)$$

where a and b are the long and short axis, respectively, of the spheroid, $\varepsilon(\omega)$ is the complex dielectric function of the metal, and L the geometric depolarization factor. The dielectric function of a metal can, as an approximation, be expressed in the Drude form as

$$\varepsilon(\omega) = 1 - \frac{\omega_p^2}{\omega(\omega + i\gamma)} \quad (2)$$

In this expression, ω_p is the bulk plasmon frequency of the metal and γ is a damping term accounting for intraband transitions (note that we neglect contributions from interband transition in this analysis for simplicity). Using the above Drude dielectric function, the quasistatic polarizability of a spheroid can be rewritten as

$$\alpha(\omega) = \frac{4\pi}{3} a^2 b \times \frac{\omega_p^2}{L\omega_p^2 - \omega^2 - i\omega\gamma} \quad (3)$$

In the MLWA formalism with dynamic depolarization and radiation damping terms, the polarizability of an oblate spheroid in its general form reads as²⁵

$$\alpha(\omega)_{\text{MLWA}} = \frac{\alpha(\omega)}{1 - \frac{\omega^2}{4\pi c^2 a} \alpha(\omega) - i \frac{\omega^3}{6\pi c^3} \alpha(\omega)} \quad (4)$$

By inserting eq 3 into eq 4, we obtain

$$\alpha(\omega)_{\text{MLWA}} = \frac{4\pi}{3} a^2 b \times \frac{\omega_p^2}{\left[L\omega_p^2 - \omega^2 \left(1 + \frac{\omega_p^2}{3c^2} ab \right) \right] - i\omega \left(\gamma + \frac{2\omega_p^2 \omega^2}{9c^3} a^2 b \right)} \quad (5)$$

The pole of the real part of eq 5 defines the localized surface plasmon frequency ω_{LSP} in the large spheroid (i.e., large a) limit as

$$\omega_{\text{LSP}}^2 = \frac{L\omega_p^2}{\frac{ab}{3c^2}\omega_p^2} = \frac{L3c^2}{ab} \quad (6)$$

Clearly ω_{LSP} becomes material independent (i.e., ω_p cancels out). To translate this expression to the parameters used to describe the nanodisks in the experiment, we define $a = D/2$ and $b = h/2$ (where D is diameter and h the height of the spheroid/nanodisks, respectively) and rewrite eq 6 as

$$\omega_{\text{LSP}}^2 = \frac{4L3c^2}{Dh} = \frac{3\pi c^2}{D^2} \quad (7)$$

by making use of the asymptotic first-order approximation of the shape factor L in the large particle limit (for $D \gg h$) where $L \approx (\pi/4) \times (h/D)$. Finally, to obtain the LSPR energy instead of frequency, eq 7 can be rewritten as

$$E_{\text{LSP}} = \hbar\omega_{\text{LSP}} = \frac{\sqrt{3\pi}\hbar c}{D} \quad (8)$$

and illustrates nicely the material independence of the LSPR energy in the large D limit and again predicts the experimentally seen $1/D$ dependence. We note that we now have taken into account the specific geometry of our system, in contrast to the more general and simple analysis presented first, which was relying solely on a field retardation argument. Using the expression from eq 8, we predict (for vacuum as the surrounding medium) a slope of 606 or 481 eV nm (for a surrounding medium with refractive index $n = 1.26$) for the $1/D$ dependence of the LSPR energy, which is reasonably close to the experimental values presented above. Mainly it is the still significant simplifying assumptions made in the above theoretical treatment, which give rise to the seen discrepancy between the slopes obtained analytically and the ones extracted from the experiment and the full MLWA calculations (where we used the exact expression for the shape factor L , instead of a linear approximation, and experimentally determined dielectric functions of the respective metals, including interband contributions, etc.).

We note that similar questions have been addressed earlier by using different theoretical formalisms, such as for IR resonances of micrometer scale metal rods where the surface impedance of different metals was

found to play a role (*i.e.*, no material independence)³⁶ and for noble metal nanorods interacting with electromagnetic radiation at optical frequencies. For the latter analysis, within the framework of antenna theory, a material dependent effective wavelength was identified.³⁷

We now turn to the experimentally observed and calculated energy dependence of the LSPR spectral line width (*i.e.*, full width at half-maximum, fwhm) for Au, Pt, and Al (Figure 5a–c). Inspecting the data in Figure 5, we note immediately the very pronounced material dependence (1 order of magnitude difference between Au and Pt) and again excellent quantitative agreement between experiment and model calculation (blue dots), except for the smallest Al disks (highest LSPR peak energy).

Following the fwhm for Au from the highest energies (smallest particles) and downward, we observe the following (Figure 5a). From 2.4 to *ca.* 2.0 eV, there is a successive decrease of the line width because the probability for interband transitions, with a threshold around 2.3 eV, successively decreases. The minimum is created because, as the particle sizes increase and LSPR energies decrease, radiation damping increases.¹⁹ Eventually a new maximum is seen around 1.2 eV, approximately when the size of the nanoparticles becomes comparable to the excitation wavelength and one enters a subradiant/quenched radiation regime,³⁸ as shown here for the first time to occur in large symmetric nanoparticles. The exact position of this maximum is predominantly determined by the conduction electron density of the material and is excellently reproduced in the model calculations. Details will be discussed below.

The observed quantitative difference between model and experiments for the fwhm (*ca.* 30 meV at low photon energy and *ca.* 80 meV at high photon energy) is attributed to shortcomings of the model, especially the failure to exactly describe the real disk-like shape of the examined nanoparticles, the simplifying assumption of a homogeneous embedding medium (*i.e.*, no substrate), and the remaining polydispersity of the particle size distribution (the latter causing experimental fwhm values to be larger than the modeled ones). The trend of an increasing difference between model and experiments, for increasing LSPR energy (decreasing particle size), is a consequence of increasing *relative* polydispersity for smaller particle size (Figure 8) and of the deviation from perfect nanodisk geometry when the particle size approaches the size of individual grains. The former contribution was verified by quantitatively estimating the inhomogeneous broadening effect for a standard deviation of the diameters of 2–3 nm with spheroid model calculations. They yielded an inhomogeneous contribution of approximately 40–50 meV to the fwhm for 50 nm Au nanodisks. This general behavior is seen also in the data for the other two metals discussed below.

For the Pt nanodisks (Figure 5b), an almost linear increase of LSPR line width is observed as a function of LSPR energy. Note that even the lowest damping for Pt

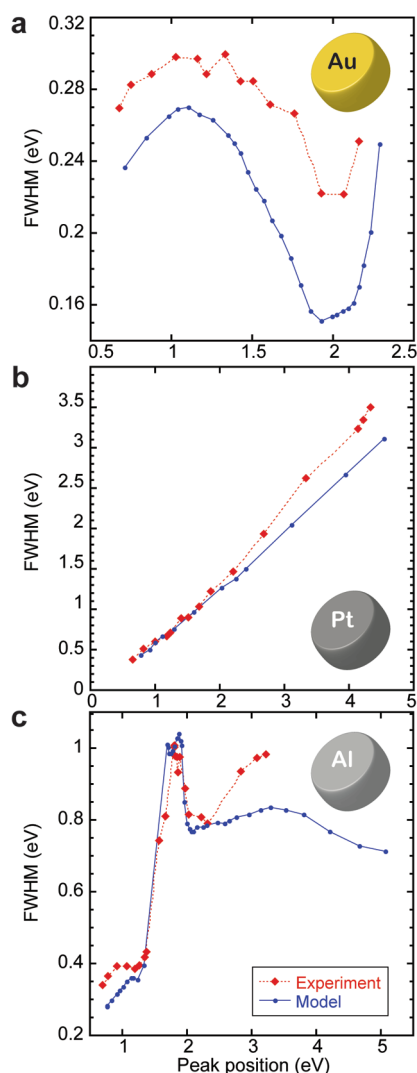


Figure 5. Energy (and size) dependence of the LSPR line width for Au (a), Pt (b), and Al (c) nanoparticles as obtained from extinction measurements (red diamonds) and calculations based on electrostatic spheroid theory (MLWA) (blue dots). The solid/dashed lines are a guide to the eye. The details are discussed in the text.

at peak energies just below 1 eV (fwhm *ca.* 0.5 eV) is larger than the highest measured damping for Au at around 1 eV (fwhm *ca.* 0.3 eV). The relative importance of radiative damping is small in this system for all particle sizes (and LSPR energies)²⁴ as a consequence of the large value of the imaginary part of the dielectric response function for Pt metal in the energy regime of interest.³⁴ The latter is connected with the high probability of e–h excitations, due to the proximity of the d band to the Fermi energy of the system. Thus, in the case of Pt, the energy dependence of the LSPR line width is dominated by the decay of the collective LSPR *via* interband excitations. The divergence between model and experimental data observed at energies >2.5 eV is attributed to the same reasons as discussed above for Au.

Turning to Al (Figure 5c), we first note that, on an absolute scale, the Al damping lies below that for Pt for

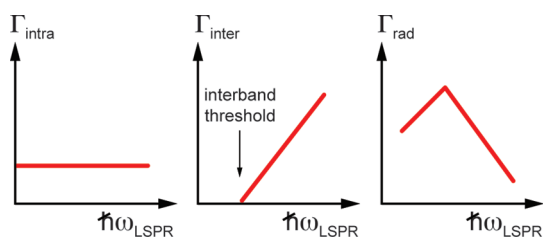


Figure 6. Schematic depiction of the expected energy (and accordingly particle size) dependence of intraband (Γ_{intra}), interband (Γ_{inter}), and radiative (Γ_{rad}) damping contributions to the total LSPR line width (for nanoparticle sizes larger than the electron mean free path). The lines indicate simplified, general trends only and not the expected exact energy dependence for a specific metal. For example, the vertical scale is arbitrary for each case and not related between the three cases.

all energies except in a narrow regime around 1.5 eV, where interband damping is comparable or even a little stronger than for Pt. Compared to Au, the Al damping is stronger everywhere except around and just below 1 eV, where the two are about equal, reflecting the absence of interband activity for both metals here. Inspecting the Al results in more detail, we note two line width maxima as a function of LSPR energy. The low energy maximum, centered at 1.5 eV, is caused by the increased interband damping of the LSPR excitation into single particle e–h excitations related to the particular band structure of Al³⁵ as discussed below in detail. This maximum is “riding” on a background of steeply increasing line width for increasing energy in the subradiant/quenched radiation regime, which extends to higher photon energies for Al compared to Au due to the higher conduction electron density (higher ω_p) in the former. The second maximum, located at ≈ 3 eV, is a transition point from the quenched radiation to the pure radiation damping dominated regime where the line width decreases as the plasmon energy increases (smaller particles imply a smaller induced dipole moment). The increasing divergence between model and experimental data, observed at energies >2.5 eV, is partly attributed to the same reasons as discussed above for Au. An additional contribution amplifying this effect in Al is the formation of a native oxide layer, which made it difficult to prepare geometrically homogeneous Al nanoparticles smaller than 50 nm. The concurrent particle roughening leads to inhomogeneous broadening of the total line width and is thus partially responsible for the deviation between experiment and theory observed in Figure 5c.

DISCUSSION

In the following section, we discuss the experimental observations, verified by spheroid theory calculations, by relating the experiments to the bulk dielectric properties of the three studied metals (see Figure 1). We start our discussion by establishing a qualitative “physical picture” of the contributions to the LSPR line width, which can be generalized to basically any metal.

Furthermore, we make, based on that picture, qualitative predictions of the energy and material/electron structure dependence of the LSPR line width in the UV–vis–NIR spectral range for our experimentally studied systems Au, Pt, and Al.

Our starting assumption for this discussion is that the total line width, Γ_{tot} for the considered particle sizes in this work is a sum of three separate contributions, $\Gamma_{\text{tot}} = \Gamma_{\text{intra}} + \Gamma_{\text{inter}} + \Gamma_{\text{rad}}$ (we neglect heterogeneous broadening effects, chemical interface damping,^{39,40} and electron–surface scattering,²⁷ as well as we assume low fluxes of the incoming photons):

- (i) Γ_{intra} : Intraband damping is related to processes where individual electrons “leave” the collective plasmonic oscillation because of diverse scattering processes within the conduction band. If the nanoparticle size D is larger than the electron mean free path λ_{mfp} , Γ_{intra} is typically ≈ 0.01 – 0.1 eV and has a very weak (practically negligible) energy dependence (at constant temperature).
- (ii) Γ_{inter} : Interband damping accounts for processes where the coherent collective electronic motion of the LSPR (energy $\hbar\omega_{\text{LSPR}}$ and momentum $q = 0$) decays into a single e–h pair (an electron in an empty state at/above the Fermi energy and a hole in the populated band) with the same energy and zero momentum. In coinage metals, having a d band positioned below the Fermi level, this effect occurs first at energies above the system-specific interband threshold (2.3 eV for Au³³). In contrast, in case of Pt, for example, the top of the 4d band is located at the Fermi energy, thus moving the threshold for LSPR decay via e–h excitation down to very small LSPR energies.³⁴
- (iii) Γ_{rad} : Radiation damping causes the collective electron motion of the LSPR to lose its energy via radiation from a time dependent induced dipole (or higher mode) which depends on the particle volume and the electron density (ω_p) in the metal. Consequently, as the nanoparticle size is increased, its volume and the size of the induced dipole increase. The total dipole moment associated with a collective plasmon mode depends on the relative phases of the individual induced electronic dipoles. If the individual nanoparticle dipoles oscillate in phase, the plasmon mode is super-radiant³⁸ and strongly radiative. In the sub-radiant regime, when the nanodisk size becomes comparable to the LSPR wavelength, the electrons begin to oscillate out of phase, the effective dipole moment and concurrently the dipole radiation strength diminishes, thus increasing the life of the LSPR excitation.

In Figure 6, we show graphically the expected trends for the energy dependence of the three contributions

to LSPR damping, Γ_{intrab} , Γ_{interb} , and Γ_{rad} , based on the above discussion.

The subradiance effect for large D can again be understood qualitatively by analyzing the polarizability of an oblate spheroid in the MLWA formalism, using a Drude form for the bulk dielectric response function, as given by eq 5 above. Here, however, to extract the line width of the resonance, we rewrite the expression for $\alpha_{\text{MLWA}}(\omega)$ as

$$\alpha(\omega)_{\text{MLWA}} = \frac{4\pi}{3} a^2 b \frac{\omega_p^2}{1 + \frac{\omega_p^2}{3c^2} ab} \times \frac{\frac{L\omega_p^2}{1 + \frac{\omega_p^2}{3c^2} ab} - \omega^2 - i\omega \frac{\gamma + \frac{2\omega_p^2\omega^2}{9c^3} a^2 b}{1 + \frac{\omega_p^2}{3c^2} ab}}{\omega_{\text{LSP}}^2 - \omega^2 - i\omega\Gamma} \quad (9)$$

In this equation, at resonance for $\omega = \omega_{\text{LSP}}$, the LSPR frequency (including the dynamic depolarization correction) is defined as

$$\omega_{\text{LSP}}^2 = \frac{L\omega_p^2}{1 + \frac{\omega_p^2}{3c^2} ab} \quad (10)$$

and Γ corresponds to the plasmon line width, which reads as

$$\Gamma = \frac{\gamma + \frac{2\omega_p^2\omega_{\text{LSP}}^2}{9c^3} a^2 b}{1 + \frac{\omega_p^2}{3c^2} ab} \quad (11)$$

Let us analyze the limiting behavior of Γ in the small ($a \ll \lambda$) and large ($a \approx \lambda$) particle limit. Since γ (intraband damping), for the systems of interest here, is much smaller than the radiative damping contribution, we neglect it in what follows and approximate the plasmon line width with the following equation instead

$$\Gamma \approx \frac{\frac{2\omega_p^2\omega_{\text{LSP}}^2}{9c^3} a^2 b}{1 + \frac{\omega_p^2}{3c^2} ab} \quad (12)$$

Since ω_p^2 is proportional to the electron density n in the nanoparticle, we see that the numerator of the above expression contains the product of electron density, the volume of the particle, and the square of the LSPR frequency.

In the *small particle limit*, where dynamic depolarization is negligible, that is, $(\omega_p^2/(3c^2)) \times ab \ll 1$, Γ is proportional to $\omega_p^2\omega_{\text{LSP}}^2 a^2 b$ and ω_{LSP}^2 is equal to $L\omega_p^2$ (see eq 10). Thus one can see (since, to a first approximation, the shape factor $L \propto b/a$, $b = h/2 = \text{const.}$, and $a = D/2$) that

$$\Gamma \propto \omega_p^4 a = \omega_p^4 \frac{D}{2} \quad (13)$$

that is, as the nanodisk diameter D increases, radiative damping increases and the particle is *super-radiant*.

In the *large particle limit*, however, the dynamic depolarization effectively reduces the number of electrons oscillating coherently and shifts the plasmon frequency into the red, thus reducing the contribution of radiative damping to the LSPR line width. This is clearly seen from eq 12, where, in the large particle limit because of $(\omega_p^2/(3c^2)) \times ab \gg 1$, $\Gamma \propto a\omega_{\text{LSP}}^2$. Furthermore, since, as shown earlier, in this limit $\omega_{\text{LSP}}^2 \propto 1/a^2$, we obtain

$$\Gamma \propto \frac{1}{a} \propto \frac{1}{D} \quad (14)$$

where the line width decreases as the particle size increases and the particle is *subradiant/radiation is quenched*. Thus, in summary, the subradiance at large particle sizes is due to the fact that dynamic depolarization has a two-fold effect on the radiative damping contribution to the LSPR line width: (i) it effectively decreases the total induced dipole moment by a factor $a^2 b / (1 + (\omega_p^2 ab)/(3c^2))$, and (ii) it shifts the LSPR frequency into red.

Further insight into the nature of the quenched radiation effect can be obtained by analyzing where the transition from super-radiance to subradiance occurs. This can be addressed by finding the maximum in Γ as a function of particle size (eq 12). Such an analysis shows that the transition between the two regimes occurs when the particle size reaches a critical value that is inversely proportional to the electron density in the system.

We now apply the above general reasoning to the three metallic systems examined in this work and qualitatively discuss the expected LSPR energy dependence of the spectral line width on that basis in order to rationalize our results presented above and as a test for our qualitative picture.

Gold. For Au nanodisks, the radiative contribution to the total damping has been shown to be significant.²⁴ Since the 5d band of Au lies 2.3 eV below the Fermi level, a threshold for interband excitation should appear around that energy. Thus, the total line width of Au LSPR excitations, as illustrated in Figure 7a, is a superposition of the three contributions described above. The line width minimum at 2.3 eV is related to the threshold for interband excitations, while the maximum at lower energies is related to quenching of the radiative contribution.

Platinum. As shown in our earlier work,²⁴ the radiative contribution to the LSPR damping in Pt nanodisks is relatively small for all disk sizes examined in this work. Furthermore, since the top of the Pt 4d band overlaps with the Fermi level, we expect that interband excitations dominate LSPR damping and thus the spectral line width already at the lowest LSPR energies.⁴¹ The predicted qualitative trend of the line width with LSPR energy is shown in Figure 7b.

Aluminum. As for Au, also in Al nanodisks the radiative contribution to the total damping is significant.¹¹

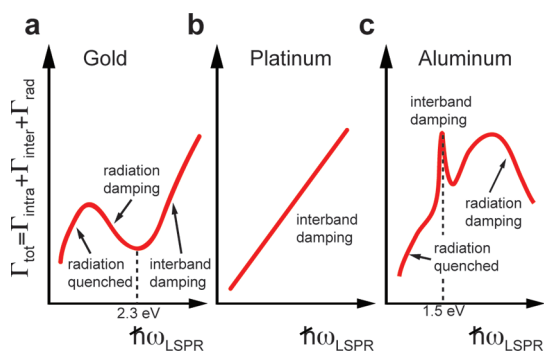


Figure 7. Schematic qualitative depictions indicating the trends for the total LSPR line width in Au, Pt, and Al nanodisks as a function of LSPR peak energy. The lines indicate simplified trends only and not the expected exact energy dependence. For example, the vertical scale is arbitrary for each case and not related between the three cases.

However, the maximum in the radiative contribution is shifted to higher LSPR energies because of the three times higher conduction electron density in Al compared to Au as derived above. This is confirmed very nicely by the experimental data (Figure 5) where the transition between the subradiance/super-radiance regimes occurs in Al at roughly three times higher LSPR energy than in Au (3.3 eV vs 1.1 eV). Furthermore, a local interband (in energy space) contribution, that is, an increase of the total line width localized around 1.5 eV, is expected due to the specific band structure of Al. The resulting expected qualitative behavior of the LSPR line width for Al nanodisks as a function of LSPR energy is shown in Figure 7c.

The above considerations and resulting trends for the LSPR line width of different nanoplasmonic materials as a function of LSPR energy (particle size) are in excellent agreement with the experimental results presented earlier in the article and can thus be used to qualitatively/mechanistically explain the made observations. Furthermore, it becomes clear that the general and rather simple concepts developed in this work, to understand the size and materials dependence of LSPR energies and damping mechanisms, are reasonable and can, due to their generic nature, be generalized to other nanoplasmonic systems/metals of technological importance.

PERSPECTIVE

The presented results for LSPR energy and line width for different materials and their relation to different damping mechanisms are relevant for several emerging and promising application areas of (nano)plasmonics. In particular, the LSPR lifetime and related damping mechanisms determine the local field enhancement around the plasmonic nanoparticles and plasmon decay channels (*i.e.*, absorption vs scattering) which are important issues in sensing^{6,7} and spectroscopic (*e.g.*, SERS¹⁷ or plasmon-enhanced fluorescence⁴²) applications since they are directly related to sensitivities and signal enhancement,

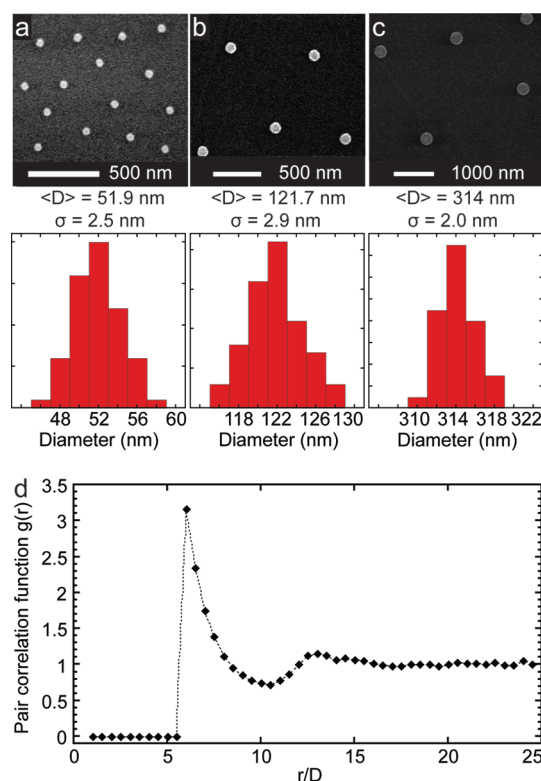


Figure 8. SEM micrographs for Au nanodisks, with average size of 52 nm (a), 122 nm (b), and 314 nm (c), obtained using the nanofabrication method described in the text. The size distribution histograms, indicating the average particle size and standard deviation, are shown below the corresponding SEM image. (d) Nanodisk pair correlation function as calculated based on nanodisks positions, which were generated with the RSA simulation algorithm and which determined the exact position of each nanodisk on the substrate surface during EBL exposure. It clearly illustrates the random order of the nanodisks on the surface with a smallest allowed center-to-center distance of 6 particle diameters D .

respectively. Both aspects (*i.e.*, dominating decay mechanisms and field enhancement) are also of great relevance in photon harvesting applications like (LSPR enhanced) photovoltaics^{43–45} where enhanced local fields⁴⁶ and efficient light scattering⁴⁷ are key ingredients. The same holds for LSPR enhanced (photo)catalysis (*e.g.*, water splitting for solar hydrogen production⁴⁸ or CO oxidation⁴⁹) where, in addition to the above-mentioned effects, also hot electrons created during the decay of the LSPR may have a beneficial effect on device performance.^{50,51}

Another field where the understanding of damping (*i.e.*, energy management after LSPR excitation) is of significant importance is nanoplasmonic heating. Plasmonic nanoparticles, strongly dependent on the choice of material as well as particle size and shape, can efficiently absorb UV, visible, or infrared light energy, which makes them very attractive nanosources of heat with a wide range of potential applications including nanoscale catalysis,⁵² magnetism and data storage,⁵³ microfluidics,⁵⁴ and medicine,¹⁸ for example, for photothermal cancer cell destruction.

Furthermore, we note that the understanding of novel (*i.e.*, other than Ag and Au) nanoplasmonic systems is expected to become increasingly more important due to, among others, lower cost (*e.g.*, Al), larger available LSPR spectral range (*e.g.*, Al¹¹), and the possibility of combining intrinsic materials properties like magnetism (*e.g.*, Ni,⁵⁵ indicating novel ways to combine nanophotonics, nanoelectronics, and nanomagnetism), hydride formation (*e.g.*, Mg, Pd¹⁴), catalytic activity (*e.g.*, Pt, Pd⁷), or phase transitions (*e.g.*, Sn¹²), *etc.*, with LSPR. Thus we believe that the presented concepts in this work, which are generic and applicable to any plasmonic nanosystems with known bulk dielectric properties, are of significant importance for the future design of nanoplasmonic devices made from a wide range of metallic systems in a wide range of applications.

CONCLUSIONS

In summary, LSPR spectral line widths and energies for disk-shaped Au, Pt, and Al nanoparticles were explored experimentally and theoretically for a broad range of nanoparticle size and concomitantly a wide energy range. This became possible by minimizing heterogeneous broadening effects by using a newly developed EBL-based preparation method yielding large surface areas covered with 2D arrangements of randomly distributed metal nanodisks with very narrow size distribution on a surface, suitable for extinction spectroscopy in a spectrophotometer with a wide spectral range. Furthermore, the random arrangement together with the large interparticle distance (center-to-center distance ≥ 6 particle diameters) minimized

particle–particle coupling effects, yielding basically single particle response. Both experimental and theoretical data showed a pronounced material dependence of the LSPR energies in the small D limit, while in the large D limit, the LSPR energy became essentially material independent. Furthermore, the contributions from radiative and nonradiative damping mechanisms to the LSPR line width for three metals with fundamentally different bulk dielectric properties were clearly identified. The observed behavior for the energy dependence of the spectral line width could be rationalized in the framework of a qualitative physical picture where the relative contributions of intraband damping, interband damping, radiation damping, and radiation quenching were considered and related to the electronic band structure of the respective metal. Furthermore, for the first time, a clear transition from a radiation damping dominated regime to a quenched radiation (subradiance) regime in very large symmetric nanoparticles was observed. The subradiance was probed by varying the conduction electron density (*i.e.*, the bulk plasma frequency) by choosing different nanoparticle materials. An excellent qualitative and quantitative agreement was obtained between the observed experimental trends and the predictions based on the spheroid model calculations, thus validating our approach to assess single particle behavior by measuring the response of a large ensemble of well-separated, identical nanodisks. The presented concepts are qualitatively generalizable to other (potentially technologically important) metallic nanosystems with known bulk dielectric properties.

METHODS

Nanofabrication and Characterization. Two-dimensional arrangements of randomly positioned metallic nanodisks (see Figure 8d for the measured pair correlation function) were fabricated on 0.7 mm thick fused silica substrates using electron-beam lithography. In short, the substrate was first covered with a resist bilayer consisting of *ca.* 60 nm ZEP520 (Nippon ZEON Ltd., Japan) on top of *ca.* 65 nm copolymer P(MMA (8.5) MAA) (MicroChem Corp., USA), which were soft-baked at 170 and 140 °C, respectively. Resist deposition was followed by resistive evaporation of a 10 nm thick Cr overcoat, which prevented charging effects during electron beam exposure, in an Edwards HPTS Auto 306 system. Matlab software (The MathWorks Inc., USA) was used to computer-generate nanodisk positions according to a random sequential adsorption scheme.⁵⁶ The size of the simulation cell was $1000D \times 1000D$, where D denotes the nanodisk diameter. Periodic boundary conditions were applied, and the minimum center-to-center distance between adjacent disks was set to $6D$. Individual nanodisks were approximated by regular polygons, where the number of corners in the polygon was adjusted to the nanodisk size (ranging from octagons for the smallest disks to hexadecagons for the largest disks). The samples were exposed in a JBX-9300FS electron-beam lithography system (JEOL Ltd., Japan) at 100 kV accelerating voltage and 2 nA beam current. Circular areas of roughly 30 mm² were patterned for each considered nanodisk size by repeatedly

exposing the simulated pattern. After electron beam exposure, the Cr charge dissipation layer was removed by dipping the samples in a ceric ammonium nitrate based chromium etch solution (Sun Chemicals A/S, Denmark) for 25 s, followed by extensive rinsing with ultrapure water and isopropyl alcohol and finally blow drying with nitrogen. Exposed resist areas were developed in two steps, first in *n*-amyl acetate (Acros Organics, USA/Belgium) and then in a mixture of methyl isobutyl ketone (MIBK, Alfa Aesar GmbH, Germany) and isopropyl alcohol in a 1:2 ratio for 65 and 75 s, respectively. After each development step, the samples were rinsed carefully with isopropyl alcohol and blow-dried. The samples were ashed in a gentle oxygen plasma (250 mTorr, 40 sccm, 20 W; Plasmatherm Batchtop m/95) for 15 s prior to electron beam evaporating *ca.* 20 nm of gold, platinum, or aluminum, in the former two cases in an AVAC HVC600 deposition system with a base pressure of 2×10^{-6} mbar and using a Lesker Spectros evaporator with a base pressure of $<1 \times 10^{-7}$ mbar in the latter case. Finally, the remaining resist and metal on top of the resist stack were removed in a two-step lift-off process in Microposit 1165 remover (Rohm and Haas Electronic Materials, USA) and acetone using mild ultrasonic agitation. The thus revealed, randomly arranged nanodisks were examined by scanning electron microscopy (JEOL JSM-6301F, Japan) and atomic force microscopy (Veeco Dimension 3000, USA). Exemplary SEM micrographs are shown in Figure 8a–c for Au nanodisks with 50, 120, and 300 nm diameter, respectively. The relatively small variations in nanodisk shape and diameter observed in these images and

supported by the corresponding size distribution histograms are representative for all reported disk sizes and chemistries (except the smallest Al nanodisks). The size distribution histograms were obtained by analyzing several SEM micrographs (ImageJ), summing up to ca. 60 analyzed disks for each size. A noticeable narrowing of the size distribution (5-fold) in comparison to samples as obtained previously by hole-mask colloidal lithography^{11,25} is found, which clearly demonstrates the usefulness of the somewhat peculiar sample preparation method presented here for studies where a large ensemble of particles is used to assess single particle properties.

Optical Extinction Spectroscopy. Optical extinction measurements were carried out in a Cary 5000 spectrophotometer by measuring optical transmission in forward direction. The spectral peak position was determined by taking a least-squares optimized polynomial fit to the data and finding the photon energy where the first derivative of the fitted polynomial was equal to zero. The spectral line width was determined from the experimental and calculated extinction spectra by multiplying the peak half-width, as measured from the resonance maximum toward the low energy side, with a factor of 2.

Spheroid Model Calculations. To scrutinize in detail the observed nanodisk size dependence of the LSPR peak position and line width for the three chosen metals theoretically and for comparison with the experimental data, we have carried out calculations based on an electrostatic spheroid model described previously.²⁵ Briefly, in this model, the nanodisks are approximated by an oblate spheroid. To calculate the polarizability of the spheroid, the internal electric field, which is a superposition of the externally applied field, the depolarization field, and the radiation field,¹⁵ is analytically determined. The dielectric response functions needed for these calculations are obtained from the literature for Au,³³ Pt,³⁴ and Al.³⁵ An effective refractive index ($n_{\text{eff}} = 1.26$) was used in the calculations by averaging the values of air ($n = 1.00$) and the glass substrate ($n = 1.52$). For Al, the same approach as presented by Langhammer *et al.*¹¹ was used for the model calculations. Namely, a 3 nm thick Al₂O₃⁵⁷ shell was used in the calculation to account for the presence of the native oxide layer formed around Al nanoparticles upon exposure to ambient conditions. The metallic core of the spheroid was modeled using the complex dielectric function of metallic Al.³⁵ The spectral line width was determined from calculated extinction spectra by multiplying the peak half-width, as measured from the resonance maximum toward the low energy side, with a factor of 2, analogous to the analysis of the experimental data.

Acknowledgment. We gratefully acknowledge fruitful discussions with V.P. Zhdanov, B. Nilsson, S. Gao, P. Apell, and Z. Yuan, the help by M. Hagberg with the Al deposition, the help by M. Holber with the RSA algorithm, and funding by the Swedish Energy Agency (Project NANO—SEE 181-1), the Foundation for Strategic Research (Project RMA 08), and the Swedish Research Council (Project 2010-4041).

REFERENCES AND NOTES

- Bohren, C. F.; Huffman, D. R. *Absorption and Scattering of Light by Small Particles*; Wiley-Interscience: New York, 1983.
- Jensen, T. R.; Duval, M. L.; Kelly, K. L.; Lazarides, A. A.; Schatz, G. C.; Van Duyne, R. P. Nanosphere Lithography: Effect of the External Dielectric Medium on the Surface Plasmon Resonance Spectrum of a Periodic Array of Silver Nanoparticles. *J. Phys. Chem. B* **1999**, *103*, 9846–9853.
- Maier, S. A.; Atwater, H. A. Plasmonics: Localization and Guiding of Electromagnetic Energy in Metal/Dielectric Structures. *J. Appl. Phys.* **2005**, *98*, 011101.
- Pendry, J. Optics: Positively Negative. *Nature* **2003**, *423*, 22–23.
- Pendry, J. Photonics—Metamaterials in the Sunshine. *Nat. Mater.* **2006**, *5*, 599–600.
- Anker, J. N.; Hall, W. P.; Lyandres, O.; Shah, N. C.; Zhao, J.; Van Duyne, R. P. Biosensing with Plasmonic Nanosensors. *Nat. Mater.* **2008**, *7*, 442–453.
- Larsson, E. M.; Langhammer, C.; Zorić, I.; Kasemo, B. Nanoplasmonic Probes of Catalytic Reactions. *Science* **2009**, *326*, 1091–1094.
- Atwater, H. A.; Polman, A. Plasmonics for Improved Photovoltaic Devices. *Nat. Mater.* **2010**, *9*, 205–213.
- Chan, G. H.; Zhao, J.; Hicks, E. M.; Schatz, G. C.; Van Duyne, R. P. Plasmonic Properties of Copper Nanoparticles Fabricated by Nanosphere Lithography. *Nano Lett.* **2007**, *7*, 1947–1952.
- Langhammer, C.; Zorić, I.; Kasemo, B.; Clemens, B. M. Hydrogen Storage in Pd Nanodisks Characterized with a Novel Nanoplasmonic Sensing Scheme. *Nano Lett.* **2007**, *7*, 3122–3127.
- Langhammer, C.; Schwind, M.; Kasemo, B.; Zorić, I. Localized Surface Plasmon Resonances in Aluminum Nanodisks. *Nano Lett.* **2008**, *8*, 1461–1471.
- Schwind, M.; Zhdanov, V. P.; Zorić, I.; Kasemo, B. LSPR Study of the Kinetics of the Liquid–Solid Phase Transition in Sn Nanoparticles. *Nano Lett.* **2010**, *10*, 931–936.
- Ekinci, Y.; Solak, H. H.; Löffler, J. F. Plasmon Resonances of Aluminum Nanoparticles and Nanorods. *J. Appl. Phys.* **2008**, *104*, 083107.
- Zorić, I.; Larsson, E. M.; Kasemo, B.; Langhammer, C. Localized Surface Plasmons Shed Light on Nanoscale Metal Hydrides. *Adv. Mater.* **2010**, *22*, 4628–4633.
- Meier, M.; Wokaun, A. Enhanced Fields on Large Metal Particles—Dynamic Depolarization. *Opt. Lett.* **1983**, *8*, 581–583.
- Moroz, A. Depolarization Field of Spheroidal Particles. *J. Opt. Soc. Am.* **2009**, *26*, 517–527.
- Moskovits, M. Surface-Enhanced Raman Spectroscopy: A Brief Retrospective. *J. Raman Spectrosc.* **2005**, *36*, 485–496.
- Gobin, A. M.; Lee, M. H.; Halas, N. J.; James, W. D.; Drezek, R. A.; West, J. L. Near-Infrared Resonant Nanoshells for Combined Optical Imaging and Photothermal Cancer Therapy. *Nano Lett.* **2007**, *7*, 1929–1934.
- Wokaun, A.; Gordon, J. P.; Liao, P. F. Radiation Damping in Surface-Enhanced Raman Scattering. *Phys. Rev. Lett.* **1982**, *48*, 957.
- Pines, D.; Nozieres, P. *Theory of Quantum Liquids*; W. A. Benjamin, Inc.: New York, 1966; Vol. 1.
- Craighead, H. G.; Niklasson, G. A. Characterization and Optical Properties of Arrays of Small Gold Particles. *Appl. Phys. Lett.* **1984**, *44*, 1134.
- Gotschy, W.; Vonmetz, K.; Leitner, A.; Aussenegg, F. R. Optical Dichroism of Lithographically Designed Silver Nanoparticle Films. *Opt. Lett.* **1996**, *21*, 1099–1101.
- Fredriksson, H.; Alaverdyan, Y.; Dmitriev, A.; Langhammer, C.; Sutherland, D. S.; Zäch, M.; Kasemo, B. Hole-Mask Colloidal Lithography. *Adv. Mater.* **2007**, *19*, 4297–4302.
- Langhammer, C.; Kasemo, B.; Zorić, I. Absorption and Scattering of Light by Pt, Pd, Ag, and Au Nanodisks: Absolute Cross Sections and Branching Ratios. *J. Chem. Phys.* **2007**, *126*, 194702.
- Langhammer, C.; Yuan, Z.; Zorić, I.; Kasemo, B. Plasmonic Properties of Supported Pt and Pd Nanostructures. *Nano Lett.* **2006**, *6*, 833–838.
- Sönnichsen, C.; Franzl, T.; Wilk, T.; von Plessen, G.; Feldmann, J.; Wilson, O.; Mulvaney, P. Drastic Reduction of Plasmon Damping in Gold Nanorods. *Phys. Rev. Lett.* **2002**, *88*, 077402.
- Hu, M.; Novo, C.; Funston, A.; Wang, H. N.; Staleva, H.; Zou, S. L.; Mulvaney, P.; Xia, Y. N.; Hartland, G. V. Dark-Field Microscopy Studies of Single Metal Nanoparticles: Understanding the Factors That Influence the Linewidth of the Localized Surface Plasmon Resonance. *J. Mater. Chem.* **2008**, *18*, 1949–1960.
- Klar, T.; Perner, M.; Grosse, S.; von Plessen, G.; Spirkel, W.; Feldmann, J. Surface-Plasmon Resonances in Single Metallic Nanoparticles. *Phys. Rev. Lett.* **1998**, *80*, 4249.
- Stietz, F.; Bosbach, J.; Wenzel, T.; Vartanyan, T.; Goldmann, A.; Träger, F. Decay Times of Surface Plasmon Excitation in Metal Nanoparticles by Persistent Spectral Hole Burning. *Phys. Rev. Lett.* **2000**, *84*, 5644.

30. Lamprecht, B.; Leitner, A.; Aussenegg, F. R. SHG Studies of Plasmon Dephasing in Nanoparticles. *Appl. Phys. B* **1999**, *68*, 419–423.
31. Wang, H.; Tam, F.; Grady, N. K.; Halas, N. J. Cu Nanoshells: Effects of Interband Transitions on the Nanoparticle Plasmon Resonance. *J. Phys. Chem. B* **2005**, *109*, 18218–18222.
32. Jensen, T.; Kelly, L.; Lazarides, A.; Schatz, G. C. Electrodynamics of Noble Metal Nanoparticles and Nanoparticle Clusters. *J. Cluster Sci.* **1999**, *10*, 295–317.
33. Johnson, P. B.; Christy, R. W. Optical Constants of Noble Metals. *Phys. Rev. B* **1972**, *6*, 4370–4379.
34. Weaver, J. H. Optical-Properties of Rh, Pd, Ir, and Pt. *Phys. Rev. B* **1975**, *11*, 1416–1425.
35. Ehrenreich, H.; Philipp, H. R.; Segall, B. Optical Properties of Aluminum. *Phys. Rev.* **1963**, *132*, 1918.
36. Rutledge, D. B.; Schwarz, S. E.; Adams, A. T. Infrared and Submillimetre Antennas. *Infrared Phys. Technol.* **1978**, *18*, 713–729.
37. Novotny, L. Effective Wavelength Scaling for Optical Antennas. *Phys. Rev. Lett.* **2007**, *98*, 266802.
38. Sonnefraud, Y.; Verellen, N.; Sobhani, H.; Vandenbosch, G. A. E.; Moshchalkov, V. V.; Van Dorpe, P.; Nordlander, P.; Maier, S. A. Experimental Realization of Subradiant, Super-radiant, and Fano Resonances in Ring/Disk Plasmonic Nanocavities. *ACS Nano* **2010**, *4*, 1664–1670.
39. Hovel, H.; Fritz, S.; Hilger, A.; Kreibitz, U.; Vollmer, M. Width of Cluster Plasmon Resonances—Bulk Dielectric Function and Chemical Interface Damping. *Phys. Rev. B* **1993**, *48*, 18178–18188.
40. Bauer, C.; Abid, J.-P.; Fermin, D.; Girault, H. H. Ultrafast Chemical Interface Scattering as an Additional Decay Channel for Nascent Nonthermal Electrons in Small Metal Nanoparticles. *J. Chem. Phys.* **2004**, *120*, 9302.
41. Pakizeh, T.; Langhammer, C.; Zorić, I.; Apell, P.; Kall, M. Intrinsic Fano Interference of Localized Plasmons in Pd Nanoparticles. *Nano Lett.* **2009**, *9*, 882–886.
42. Tam, F.; Goodrich, G. P.; Johnson, B. R.; Halas, N. J. Plasmonic Enhancement of Molecular Fluorescence. *Nano Lett.* **2007**, *7*, 496–501.
43. Ferry, V. E.; Munday, J. N.; Atwater, H. A. Design Considerations for Plasmonic Photovoltaics. *Adv. Mater.* **2010**, *22*, 4794–4808.
44. Hagglund, C.; Apell, S. P.; Kasemo, B. Maximized Optical Absorption in Ultrathin Films and Its Application to Plasmon-Based Two-Dimensional Photovoltaics. *Nano Lett.* **2010**, *10*, 3135–3141.
45. Kulkarni, A. P.; Noone, K. M.; Munechika, K.; Guyer, S. R.; Ginger, D. S. Plasmon-Enhanced Charge Carrier Generation in Organic Photovoltaic Films Using Silver Nanoprisms. *Nano Lett.* **2010**, *10*, 1501–1505.
46. Häggglund, C.; Zäch, M.; Kasemo, B. Enhanced Charge Carrier Generation in Dye Sensitized Solar Cells by Nanoparticle Plasmons. *Appl. Phys. Lett.* **2008**, *92*, 013113.
47. Hagglund, C.; Zäch, M.; Petersson, G.; Kasemo, B. Electromagnetic Coupling of Light into a Silicon Solar Cell by Nanodisk Plasmons. *Appl. Phys. Lett.* **2008**, *92*, 053110.
48. Thimsen, E.; Le Formal, F.; Grätzel, M.; Warren, S. C. Influence of Plasmonic Au Nanoparticles on the Photoactivity of Fe₂O₃ Electrodes for Water Splitting. *Nano Lett.* **2011**, *11*, 35–43.
49. Hung, W. H.; Aykol, M.; Valley, D.; Hou, W.; Cronin, S. B. Plasmon Resonant Enhancement of Carbon Monoxide Catalysis. *Nano Lett.* **2010**, *10*, 1314–1318.
50. Zhdanov, V. P.; Kasemo, B. Specifics of Substrate-Mediated Photo-Induced Chemical Processes on Supported nm-Sized Metal Particles. *J. Phys.: Condens. Matter* **2004**, *16*, 7131–7141.
51. Mulugeta, D.; Kim, K. H.; Watanabe, K.; Menzel, D.; Freund, H. J. Size Effects in Thermal and Photochemistry of NO₂ on Ag Nanoparticles. *Phys. Rev. Lett.* **2008**, *101*, 4.
52. Cao, L.; Barsic, D. N.; Guichard, A. R.; Brongersma, M. L. Plasmon-Assisted Local Temperature Control To Pattern Individual Semiconductor Nanowires and Carbon Nanotubes. *Nano Lett.* **2007**, *7*, 3523–3527.
53. Challener, W. A.; Peng, C.; Itagi, A. V.; Karns, D.; Peng, W.; Peng, Y.; Yang, X.; Zhu, X.; Gokemeijer, N. J.; Hsia, Y. T.; et al. Heat-Assisted Magnetic Recording by a Near-Field Transducer with Efficient Optical Energy Transfer. *Nat. Photonics* **2009**, *3*, 220–224.
54. Liu, G. L.; Kim, J.; Lu, Y.; Lee, L. P. Optofluidic Control Using Photothermal Nanoparticles. *Nat. Mater.* **2006**, *5*, 27–32.
55. Valev, V. K.; Silhanek, A. V.; Gillijns, W.; Jeyaram, Y.; Paddubrouskaya, H.; Volodin, A.; Biris, C. G.; Panoiu, N. C.; De Clercq, B.; Ameloot, M.; et al. Plasmons Reveal the Direction of Magnetization in Nickel Nanostructures. *ACS Nano* **2011**, *5*, 91–96.
56. Hinrichsen, E. L.; Feder, J.; Jøssang, T. Geometry of Random Sequential Adsorption. *J. Stat. Phys.* **1986**, *44*, 793–827.
57. Palik, E. D. *Handbook of Optical Constants of Solids II*; Academic Press: New York, 1991.